RESEARCH ARTICLE
PLANETARY SCIENCES

Earth and Planetary Physics
8: 890–898, 2024
doi: 10.26464/epp2024067

Research on internal gravity waves in the Martian atmosphere based on Tianwen-1 and Mars Global Surveyor occultation data

Luo Xiao[1,2], CunYing Xiao[1,2*], Xiong Hu[3,4], ZeWei Wang[1,2], and XiaoQi Wu[1,2]

[1]Institute for Frontiers in Astronomy and Astrophysics, Beijing Normal University, Beijing 102206, China;

[2]School of Physics and Astronomy, Beijing Normal University, Beijing 100875, China;

[3]State Key Laboratory of Space Weather, National Space Science Center, Chinese Academy of Sciences, Beijing 100045, China;

[4]Key Laboratory of Science and Technology on Environmental Space Situation Awareness, National Space Science Center, Chinese Academy of Sciences, Beijing 100190, China

Key Points:

- Radio occultation data from China's Tianwen-1 probe, with a high vertical resolution of ~0.3 km, is first used to study internal gravity waves (IGWs) in the Martian atmosphere.
- The key parameters of the IGW extracted from Tianwen-1 indicate that this IGW is a low-frequency gravity wave with a dominant vertical wavelength of 12.6 km.
- Comparison results show that the IGW activity detected by Tianwen-1 is stronger, with a greater temperature perturbation and less dissipation than that of MGS.

Citation: Xiao, L., Xiao, C. Y., Hu, X., Wang, Z. W., and Wu, X. Q. (2024). Research on internal gravity waves in the Martian atmosphere based on Tianwen-1 and Mars Global Surveyor occultation data. *Earth Planet. Phys.*, *8*(6), 890–898. http://doi.org/10.26464/epp2024067

Abstract: Internal gravity waves (IGWs) are critical in driving Martian atmospheric motion and phenomena. This study investigates Martian IGWs by using high-resolution data from China's Tianwen-1 mission and the National Aeronautics and Space Administration's Mars Global Surveyor (MGS) by the radio occultation (RO) technique. Key IGW parameters, such as vertical and horizontal wavelengths, intrinsic frequency, and energy density, are extracted based on vertical temperature profiles from the Martian surface to ~50 km altitude. Data reveal that the Martian IGWs are predominantly small-scale waves, with vertical wavelengths between 6 and 13 km and horizontal wavelengths extending to thousands of kilometers. These waves propagate almost vertically and exhibit low intrinsic frequencies close to the inertial frequency, with the characteristic of low-frequency inertial IGWs. Tianwen-1 data indicate stronger IGW activity, higher energy density, and less dissipation than MGS data in the northern hemisphere. Moreover, MGS data in the southern hemisphere show higher buoyancy frequencies and lower vertical wavelengths, suggesting more stable atmospheric conditions conducive to IGW propagation. These extracted IGW characteristics can enhance our understanding of the atmospheric dynamics on Mars and contribute valuable information for parameterization in global circulation models.

Keywords: internal gravity waves; Mars; Tianwen-1; Mars Global Surveyor; radio occultation

1. Introduction

In a stratified fluid characterized by a continuously varying density profile, external perturbations that induce deviations from the hydrostatic equilibrium state result in oscillatory motion governed by the restoring forces of gravitational buoyancy, thereby facilitating the generation of gravity waves (GWs). If the process occurs in an incompressible fluid (e.g., the ocean), GWs propagate mainly in the horizontal plane as vertically traveling waves are reflected at the upper and lower boundaries. In the atmosphere, gravity waves can propagate horizontally and vertically. To differentiate, the former GWs, which can only propagate horizontally, are surface waves. The latter are internal waves, that is, internal GWs (IGWs; Medvedev and Yiğit, 2019).

During the propagation of IGWs, the energy and momentum carried by the IGWs power atmospheric motion, driving kinds of atmospheric phenomena and even global circulation, which play substantial roles in planetary atmospheric dynamics. The important role of IGWs in atmospheric dynamics and global circulation has been widely studied on Earth, such as Xiao CY and Hu X (2010) revealing the monthly mean global morphologies of potential energy density from stratospheric GWs by observations of COSMIC (Constellation Observing System for Meteorology, Ionosphere and Climate) GPS RO. IGWs exist extensively on Earth and commonly on other planets with stable atmospheric stratification, such as Mars and Jupiter (Lian Y and Yelle, 2019; Ji QQ et al., 2022).

First author: L. Xiao, 202221160026@mail.bnu.edu.cn
Correspondence to: C. Y. Xiao, xiaocunying@bnu.edu.cn
Received 11 JUN 2024; Accepted 03 SEP 2024.
First Published online 29 OCT 2024.

The amplitude of IGWs generated in the lower atmosphere increases with altitude until they reach a critical value, saturate, and break up, causing turbulence and affecting momentum transport. Several accidents during high-altitude aircraft flights have been attributed to stratospheric turbulence caused by unexpected mountain waves (Skopovi and Akylas, 2007). Mountain waves are generated by airflow disturbance as the airflow passes over mountainous terrain. Topography is the primary excitation source for mountain waves and IGWs. Mars has very large topographic characteristics and strong winter zonal jets, enabling much stronger topographically induced IGWs (Fritts et al., 2006).

Radio occultation technology is an important means of Mars exploration. For example, the Mars Global Surveyor (MGS) provided profiles of pressure and temperature in the lower atmosphere of Mars for several years. The MAVEN (Mars Atmosphere and Volatile EvolutioN) spacecraft obtained the electron density profiles and refractivity profiles in the middle and lower layers of Mars, which proved that the neutral atmosphere layer is below approximately 80 km, whereas the ionosphere is above approximately 80 km (Zhang SJ et al., 2009). We have summarized the progress of radio occultation exploration of Mars (Xiao et al., 2024). The study of IGWs on Mars is primarily conducted by analyzing these RO atmospheric temperature profiles. Creasey et al. (2006) calculated the energy density of the corresponding wave for each vertical temperature profile derived from the National Aeronautics and Space Administration's (NASA's) MGS RO measurement, obtaining the global distribution of wave activities. Using the same data, Ando et al. (2012) obtained the vertical wavenumber spectra of Martian GWs at ~3–32 km, which were basically consistent with the theoretical spectra of saturated GWs in the Earth's atmosphere. From multiple vertical temperature profiles of the MGS, Gubenko et al. (2015) determined the characteristics of Martian atmospheric IGWs as well as key parameters, such as frequency, wavelength, and energy density.

China's first Mars exploration mission, Tianwen-1, was successfully launched on July 23, 2020. It entered the orbit around Mars in February 2021 and conducted the first RO experiment with X-band radio signals on August 5, 2021, obtaining data on the ionosphere and atmosphere on Mars (Hu X et al., 2022). This experiment revealed that the Tianwen-1 RO data are scientifically reliable and helpful for further research on the atmosphere and space weather of Mars. The authors also found distinct wavelike structures from the temperature profile, indicating that Mars has rich atmospheric wave activities. Tianwen-1's RO neutral atmosphere data have a higher vertical resolution of ~0.3 km than previous Mars data, allowing for a more detailed analysis of IGWs.

To better understand the Martian atmospheric dynamics, we extract the IGW parameters based on RO data from Tianwen-1 and from the MGS as contrasts and complements. First, we introduce the data and methods of extracting IGW parameters through vertical temperature profiles in Section 2. We then analyze the characteristics of IGWs by Tianwen-1, compared with those by the MGS in Section 3. Section 4 presents the conclusions.

2. Data and Methods

2.1 Data

The first RO experiment was conducted by Tianwen-1 with signals on August 5, 2021 (Hu X et al., 2022). Tianwen-1 transmits X-band radio signals received by the Shanghai Observatory, establishing a one-way single-frequency link in the X-band to conduct radio occultation experiments. The location of the occulted path closest to the surface of Mars is estimated as (66.03°N, −161.49°E), when the solar zenith angle is 87.7° and the local time is 22.7 h. The season of the RO event is the spring of Mars, with a Martian solar longitude of L_s = 81.3°. Tianwen-1 obtained atmospheric density and temperature data from the Martian surface to ~50 km altitude. In contrast to the MGS, which has a vertical resolution of approximately 1 km, Tianwen-1 achieves a significantly improved vertical resolution of about 0.3 km.

Radio occultation data from the MGS are also selected for comparison with RO data from Tianwen-1. The MGS was launched in 1996 and has achieved nearly a decade of RO observations, detecting data on pressure and temperature in the lower atmosphere. During the years of operation, a total of 5600 RO profiles were returned, and the detection position was mostly distributed in the northern hemisphere, covering the position of the corresponding data from Tianwen-1.

The physical state and temperature of the upper atmosphere depend largely on the condition and thermal structure of the lower atmosphere (Gröller et al., 2018). In this article, we mainly report on our study of IGWs in the lower atmosphere of Mars. Because GW activities on Mars vary substantially with season and latitude but not much with longitude (Creasey et al., 2006), we choose the MGS profiles that differ by ±2.5° in latitude, ±10° in longitude, and ±5° in L_s from the Tianwen-1 profile to reduce the effects of different geographic locations and seasons on the GW activities. According to these criteria, we select some MGS profiles for the preliminary analysis and finally show three representative ones. Two of them are the 0334i12b.tps profile observed at 08:12 on November 29, 2000, which corresponds to a latitude of 66.11°N, a longitude of 201.28°, and a L_s value of 82.51°; and the 0339l46b.tps profile observed at 11:46 on December 4, 2000, which corresponds to a latitude of 66.81°, a longitude of 196.86°, and a L_s value of 84.77°.

It is well known that considerable differences in topography exist between the northern and southern hemispheres of Mars. Le HJ et al. (2022) noted that the large hemispheric differences in Martian topography and the subsequent effects of dust storms could lead to substantial wave processes, which could affect the lower atmosphere. Considering the differences in topography and magnetic field between the northern and southern hemispheres, we select a few more profiles from the relatively strong magnetic field region in the southern hemisphere (Acuña et al., 1999). One representative profile is shown: the 9134p06a.tps profile observed at 15:06 on May 14, 1999, which corresponds to a latitude of −68.48°N and a longitude of 170.76°, with a L_s value of 138.74°.

2.2 Methods

The extraction process of IGW parameters is mainly done with reference to Gubenko et al. (2008) and has the advantage that various parameters of IGWs can be extracted simply by analyzing a single temperature profile. The method is universal and applicable not only to the Earth's atmosphere (Gubenko et al., 2008), but

also to other planetary atmospheres, such as Mars (Gubenko et al., 2015).

To understand the spatial scales of IGWs, we extract their vertical and horizontal wavelengths. By applying the Lomb–Scargle spectral analysis method to the temperature perturbation ($T'_0 = T - \bar{T}$), the main wavelength λ_z of the wave perturbation can be determined, where T is the measured temperature and $\bar{T}$ is the background temperature, which is usually obtained by the polynomial fitting method in the research on GWs (Wang L and Geller, 2003; He Y et al., 2021). Fitting the background temperature with polynomials of different orders causes slight differences in the temperature perturbation. For instance, a linear fit may artificially increase the perturbation amplitude, as illustrated in Figure 1b. Given that the vertical wavelengths of GWs on Mars reported in previous studies generally do not exceed 15 km (Creasey, 2012; Saunders et al., 2021), we choose to filter T'_0 with a vertical bandpass filter of 3–15 km to eliminate the effects of large-scale waves and obtain filtered temperature perturbation T' (Zhang J et al., 2023). The differences in the filtered temperature perturbations obtained by different polynomials are small, and the filtered perturbations are the focus of this article. The IGW parameters extracted by fitting the background temperature with polynomials of different orders are also quite close. Considering that excessively high orders of fitting may lead to overfitting effects, we choose to directly use the commonly used third-order polynomial for fitting in the subsequent parameter extraction. Because edge effects occur during the fitting process, the data within the top and bottom 2.5 km of the height range are excluded in the subsequent parameter extraction. The window function and a 95% confidence level are added to reduce the problem of spectral leakage. The horizontal wavelength λ_h can be determined by $\lambda_h = 2\pi/k_h$. The horizontal wavenumber k_h can be calculated by the dispersion relation of the IGWs,

$$k_h^2 = \left(m^2 + \frac{1}{4H^2}\right) \cdot (\omega^2 - f^2)/N^2, \tag{1}$$

in Nappo (2013), where m represents the vertical wavenumber, $m = 2\pi/\lambda_z$, and H denotes the scale height of the Martian atmosphere, obtained by fitting the atmospheric density or pressure profile. The intrinsic frequency ω is the IGW frequency mentioned below, and the inertial frequency $f = 2\Omega\sin\varphi$, where $\Omega = 7.11 \times 10^{-5}$ rad/s is the angular velocity of Mars' rotation around its axis and φ is the latitude (Gubenko et al., 2015). The square of buoyancy frequency N^2 is a measure of atmospheric static stability, determined by the background temperature profile (Liu X et al., 2020), that is,

$$N^2 = \frac{g}{\bar{T}}\left(\frac{\partial \bar{T}}{\partial z} + \frac{g}{C_p}\right),$$

where g is free fall acceleration near the Martian surface, z is altitude, C_p is the specific air heat capacity at constant pressure. Only when $N^2 > 0$ is the atmosphere stably stratified and the wave motion possible.

With the aim of gaining a better understanding of the temporal scales of IGWs, their intrinsic frequency and period can be extracted. Because RO detection cannot obtain the data on atmospheric wind speed directly, we cannot directly extract the horizontal wind speed perturbation caused by IGWs and the horizontal kinetic energy density. The intrinsic frequency ω of IGWs cannot be calculated directly by E_{kh} and E_p, as shown by Geller and Gong J (2010), so we refer to the method of Gubenko et al. (2008) for ω. This method is based on the premise that the relative amplitude a_e of the wave reaches the threshold amplitude a of the shear instability, that is, $a = a_e$, where

$$a_e = \frac{gm}{N^2} \cdot \frac{|T'|}{\bar{T}} = \frac{2\pi g}{\lambda_z N^2} \cdot \frac{|T'|}{\bar{T}}, \tag{2}$$

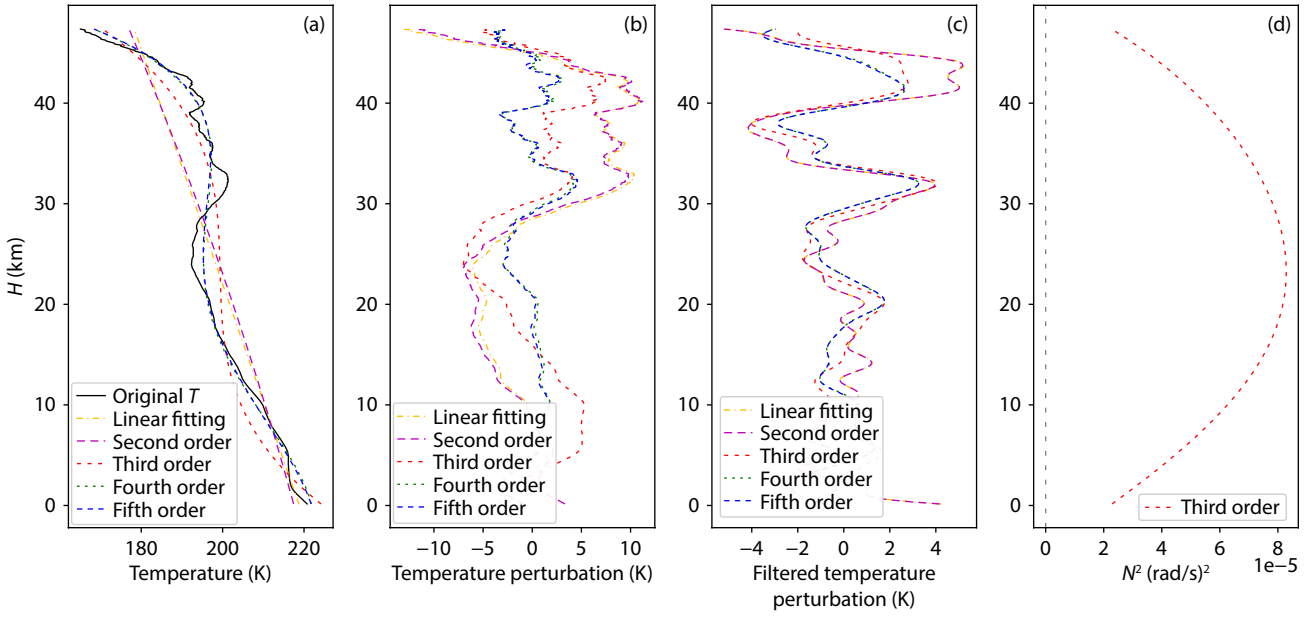

Figure 1. (a) Temperature T, (b) temperature perturbation T'_0, (c) filtered temperature perturbation T', and (d) the square of buoyancy frequency N^2 with altitude for Tianwen-1.

$$a = 2 \cdot \left(1 - \frac{f^2}{\omega^2}\right)^{\frac{1}{2}} \cdot \left[1 + \left(1 - \frac{f^2}{\omega^2}\right)^{\frac{1}{2}}\right]^{-1}, \quad (3)$$

where $|T'|$ represents the amplitude of IGWs, which can be ascertained through sinusoidal fitting. If $0 < a_e < 1$, we consider the perturbations to be caused by saturated IGWs. Conversely, if $a_e \geq 1$, we associate the observed fluctuations with regular thin layers or turbulence. According to $a = a_e$ and Equations (2) and (3), we can determine the intrinsic frequency ω and period $T(2\pi/\omega)$ of IGWs.

We can determine the direction of the wave propagation by

$$\tan\Phi_0 = \frac{m}{k_h} = \frac{\lambda_h}{\lambda_z},$$

where Φ_0 is the angle between the wave vector direction and the horizontal plane. The speed and direction of wave energy transmission are described by the group velocity, and the speed of a constant phase point along the direction of the traveling wave is described by the phase velocity. Referring to the calculation method of Gubenko et al. (2011), we can calculate the group velocity $\left|C_{gh}^{\text{in}}\right|$, $\left|C_{gz}^{\text{in}}\right|$ and the intrinsic phase velocity $\left|C_{ph}^{\text{in}}\right|$, $\left|C_{pz}^{\text{in}}\right|$:

$$\left|C_{gh}^{\text{in}}\right| = \frac{\partial\omega}{\partial k_h} = \left|C_{ph}^{\text{in}}\right| \cdot \left(1 - \frac{f^2}{\omega^2}\right) = \frac{N}{m} \cdot \sqrt{1 - \frac{f^2}{\omega^2}}, \quad (4)$$

$$\left|C_{gz}^{\text{in}}\right| = \frac{\partial\omega}{\partial m} = \left|C_{pz}^{\text{in}}\right| \cdot \left(1 - \frac{f^2}{\omega^2}\right) = \frac{|k_h|\,N}{m^2} \cdot \sqrt{1 - \frac{f^2}{\omega^2}}. \quad (5)$$

We can ascertain the activity intensity of IGWs by calculating the kinetic and potential energy density. The higher the energy, the stronger the wave activity. Because wave energy is periodic in space and time, it is more useful to discuss average values rather than local values (Nappo, 2013). Kinetic and potential energy densities E_k and E_p can be calculated by using the following formulas:

$$E_k = \frac{1}{2}\left(\overline{u'^2} + \overline{v'^2} + \overline{w'^2}\right) = \frac{1}{4}\left(|u'|^2 + |v'|^2 + |w'|^2\right), \quad (6)$$

$$E_p = \frac{1}{2}\frac{g^2}{N^2}\overline{\left(\frac{T'}{\overline{T}}\right)^2} = \frac{1}{4}\frac{g^2}{N^2}\left|\frac{T'}{\overline{T}}\right|^2, \quad (7)$$

where u', v', w' correspond to the zonal, meridional, and vertical velocity perturbations induced by the wave, respectively. They can be obtained by the polarization equation of the IGWs.

3. Results and Discussion

3.1 Results of Tianwen-1

As shown in Figure 1a, the temperature decreases with altitude from the surface to approximately 24 km, similar to the pattern observed in Earth's troposphere. Between 25 and 33 km, the temperature increases with altitude, which is referred to as an inversion layer. In the atmosphere, the inversion layer exhibits greater stability than usual, indicated by a higher value of N^2, as shown in Figure 1d. In Figure 1b, the trends of temperature perturbations fitted by different polynomials exhibit consistency, and in Figure 1c, the filtered temperature perturbations are much more similar, indicating that the polynomial fitting order has minimal impact on the IGWs within the 3–15 km range studied. The perturbation amplitude of the linear fit is significantly larger, suggesting that a poorly fitting curve artificially increases the amplitude, which is consistent with the view of Creasey (2012). The good fit of the third-order polynomial in Figure 1 indicates that using the third-order polynomial in this study is appropriate. The comparison between Figures 1b and 1c reveals that the filtered perturbations are significantly reduced, indicating that in addition to GWs with vertical wavelengths of 3–15 km, larger scale waves, such as tides and planetary waves, exist and that the temperature perturbations they induce are also important.

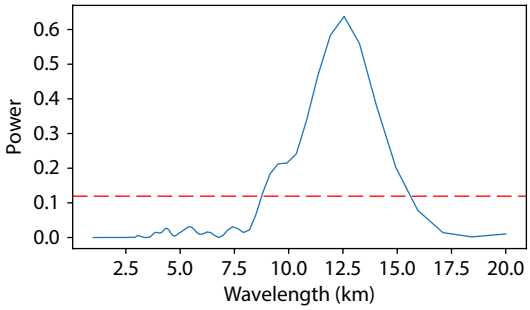

Figure 2. Lomb–Scargle power spectrum of the temperature perturbation T' of Tianwen-1 with a 95% confidence level.

From Figure 2, the main energy distribution of the IGW can be observed to lie within the range of ~9–15 km. The narrow single-peak structure indicates the quasi-periodic nature of this temperature perturbation, which may be caused by the propagation of a monochromatic wave that is saturated because of shear atmospheric instability (Fritts and Alexander, 2003). The dominant vertical wavelength λ_z of the IGW is approximately 12.6 km. The horizontal wavelength λ_h is approximately 5212 km, which largely coincides with our expected horizontal wavelength of hundreds or even thousands of kilometers. The horizontal wavelength is calculated from the dispersion relation of the IGWs and $\lambda_h = 2\pi/k_h$. This relation has been used for many years and is reliable. The parameters used are those in Equation (1) and are calculated strictly according to the method. Errors are assessed in Table 1, and the parameters are considered reasonable in this study.

The amplitude $|T'|$ represents the intensity of the IGW activity. By sinusoidal fitting, we can determine that the amplitude of the IGW is 1.90 K, as shown in Figure 3. Substituting the median value of N^2 into Equation (1) yields $a_e = 0.261$. Subsequently, we can determine that the intrinsic frequency of the IGW is 1.31×10^{-4} rad/s, close to the inertial frequency ($\omega \sim f$), which is a typical low-frequency IGW, also known as an inertial IGW. The corresponding period is 13.3 h. The angle Φ_0 between the direction of the wave vector of this IGW and the horizontal plane is 89.86°, implying that the IGW propagates almost vertically. Calculations show that $\left|C_{gh}^{\text{in}}\right| = 2.48$ m/s, $\left|C_{gz}^{\text{in}}\right| = 5.97 \times 10^{-3}$ m/s, $\left|C_{ph}^{\text{in}}\right| = 109$ m/s, $\left|C_{pz}^{\text{in}}\right| = 0.264$ m/s, with the group velocity significantly slower.

With $E_k = 94.1$ J/kg and $E_p = 4.64$ J/kg determined, the energy density of the IGW can be obtained. During the calculation, we find that the vertical velocity perturbation $|w'|$ is two or three orders of magnitude smaller than the horizontal wind perturbation

Table 1. Parameters of the IGWs and their uncertainties.

IGW parameter	Profile			
	1	2	3	4
	Tianwen-1 2021-08-05 (66.03°N, 198.51°E) Altitude ~0.15–47.45 km	MGS 2000-11-29 (66.11°N, 201.28°E) ~3.65–39.35 km	MGS 2000-12-04 (66.81°N, 196.86°E) ~4.3–40.0 km	MGS 1999-05-14 (−68.48°N, 170.76°E) ~3.0–23.5 km
L, km	47.3	35.7	35.7	20.5
$N^2_{\rm med}$, 10^{-5}rad^2/s^2	6.79 ± 1.26	5.16 ± 0.77	5.19 ± 0.71	11.08 ± 2.09
λ_z, km	12.6 ± 0.15	9.3 ± 0.63	10.4 ± 0.67	6.7 ± 0.38
λ_h, km	5212 ± 1245	4285 ± 966	5273 ± 1121	3404 ± 915
$\lvert T'\rvert$, K	1.90 ± 0.05	0.76 ± 0.05	0.80 ± 0.06	1.08 ± 0.07
a_e, rel.units	0.261 ± 0.049	0.211 ± 0.038	0.194 ± 0.033	0.268 ± 0.055
ω/f	1.011	1.007	1.006	1.012
ω, 10^{-4}rad/s	1.31 ± 0.006	1.31 ± 0.004	1.31 ± 0.002	1.34 ± 0.010
Φ_0, deg	89.86	89.88	89.89	89.89
$\lvert C^{\rm in}_{ph}\rvert$, m/s	109 ± 25.7	89.6 ± 20.0	111 ± 23.3	72.7 ± 19.2
$\lvert C^{\rm in}_{pz}\rvert$, 10^{-3}m/s	264 ± 3.5	194 ± 13.1	218 ± 14.0	143 ± 8.3
$\lvert C^{\rm in}_{gh}\rvert$, m/s	2.48 ± 0.58	1.25 ± 0.27	1.28 ± 0.27	1.73 ± 0.46
$\lvert C^{\rm in}_{gz}\rvert$, 10^{-3}m/s	5.97 ± 2.60	2.71 ± 1.10	2.52 ± 0.97	3.42 ± 1.67
$\lvert u'\rvert$, m/s	13.8 ± 1.3	12.7 ± 1.3	14.1 ± 1.4	11.2 ± 1.3
$\lvert v'\rvert$, m/s	13.6 ± 1.3	12.6 ± 1.3	14.1 ± 1.4	11.1 ± 1.3
$\lvert w'\rvert$, 10^{-3}m/s	33.2 ± 6.4	27.4 ± 5.3	27.8 ± 5.1	22.1 ± 4.9
E_k, J/kg	94.1 ± 18.6	79.5 ± 17.3	99.4 ± 20.7	62.3 ± 15.3
E_p, J/kg	4.64 ± 0.86	1.25 ± 0.21	1.34 ± 0.21	2.26 ± 0.45
E_k/E_p	20.3	63.5	74.4	27.6
H, km	10.8	9.9	10.2	7.1
H_{pv}, km	63.7	12.3	10.6	17.8

($\lvert u'\rvert$ and $\lvert v'\rvert$), indicating that the primary source of the IGW kinetic energy (E_k) is the horizontal wind perturbation. This aligns with the findings of Ratnam et al. (2008) on IGWs, where the vertical wind perturbation contributed only 0.7% to the total kinetic energy and was deemed negligible. The horizontal kinetic energy density is sensitive to low-frequency GWs, whereas the vertical kinetic energy density is more responsive to high-frequency GWs (Geller and Gong J, 2010). Namely, for the low-frequency inertial GWs, the vertical wind perturbation is significantly smaller than the horizontal wind perturbation. According to the perspective of Geller and Gong J (2010), the IGW should be a low-frequency IGW, which is consistent with our calculation.

Since many of the parameters discussed above are derived from temperature profiles, it is essential to conduct an error assessment. According to the uncertainty formulas provided by Gubenko et al. (2008), when a_e converges to 1, the relative uncertainty of parameters such as ω, $C^{\rm in}_{pz}$, $\lvert v'\rvert$, $\lvert w'\rvert$, λ_h, $C^{\rm in}_{gz}$ would be large. Therefore, we consider this when choosing profiles in the MGS database. Rather than selecting profiles with large temperature perturbations, we prioritize those with relatively mild perturbations to minimize uncertainty under this method. By substituting Tianwen-1's data height range of L = 47.3 km and relevant parameters into the uncertainty formulas, we obtain uncertainties of $\delta\lambda_z/\lambda_z \approx 1.2\%, \delta N^2/N^2 \approx 18.5\%, \delta a_e/a_e \approx 18.7\%$. Similarly, uncertainties for other parameters can be calculated.

To quantitatively describe the dissipation of IGWs with altitude, we follow the approach of Zhao WB et al. (2022) and introduce the concept of volumetric potential energy density

$$E_{pv} : E_{pv} = \rho \cdot E_p,$$

where

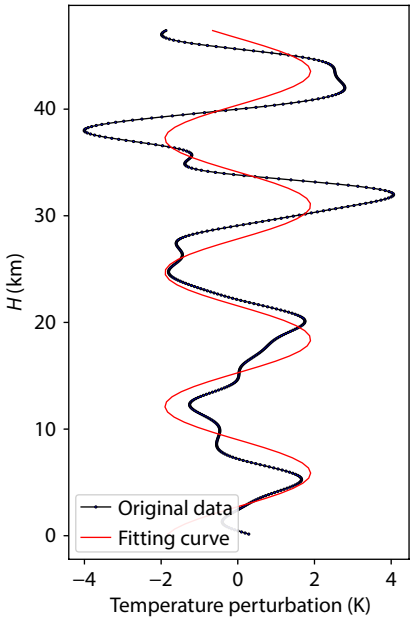

Figure 3. Sinusoidal fitting of the temperature perturbation of Tianwen-1.

$$E_p(z) = E_p(z_0) \cdot \exp\left(\frac{z - z_0}{H_p}\right), E_{pv}(z) = E_{pv}(z_0) \cdot \exp\left(\frac{z_0 - z}{H_{pv}}\right).$$

For conservative GWs, $H_p = H$, where $H = -(\mathrm{d}\ln\rho/\mathrm{d}z)^{-1}$. Potential energy density E_p increases exponentially with altitude, whereas volumetric potential energy density E_{pv} remains constant regardless of altitude. When $H_p > H$, the growth rate $1/H_p$ of the GW is lower than the growth rate $1/H$ of a conservative GW, indicating wave dissipation. In this case, H_{pv} is positive. The larger the value of H_p, the greater the dissipation is, and the corresponding H_{pv} is positive but decreases as dissipation becomes more pronounced. By fitting the atmospheric density ρ, E_p, and E_{pv} profile, as shown in Figure 4, the parameters corresponding to IGW of the Tianwen-1 profile are determined: H = 10.8 km, H_p = 11.7 km, and H_{pv} = 63.7 km. The variable $H_p > H$ indicates that this IGW is dissipating, likely due to the transfer of its energy into the background atmosphere. The variable H_{pv} = 63.7 km indicates that the E_{pv} of IGW decreases to 1/e of its initial value at 63.7 km above the reference point, suggesting a relatively weak dissipation.

3.2 Results of the MGS and Comparisons with Tianwen-1

Unlike Tianwen-1, which exhibits a distinct inversion layer between 25 and 33 km, the temperature of the MGS decreases steadily with altitude, showing no evidence of inversion layer. Because of the difference in temperature profiles, the variation trends of N^2 with altitude for the MGS are also different, initially decreasing and then increasing. In Figures 5b and 6b, the perturbation profiles before and after filtering are similar, indicating that the temperature perturbations caused by other scale waves are not significant, which are also different from Tianwen-1. The perturbation amplitude of the northern hemisphere IGWs detected by the MGS is smaller than that of Tianwen-1, that is, the gravity wave activity is weaker, which may be related to the local weather conditions at the time. For example, during SSWs, gravity wave activity intensifies with higher energy density (E_p), whereas after SSWs, E_p usually decreases (Zeng XY and Zhong G, 2024). Dust is one of the excitation sources of atmospheric fluctuations, which vary in different degrees during dust storms (Wu ZP et al., 2021). In both Figures 5c and 6c, local minima are observed at 16 and 18 km, respectively, indicating the existence of dynamic instability near corresponding altitudes.

The IGWs have vertical wavelengths of 9.3 and 10.4 km, with corresponding horizontal wavelengths of 4285 and 5273 km, respectively. Their relative amplitudes and energy densities are smaller, indicating that their activity intensities are weaker. The intrinsic frequency and period are nearly the same as those of Tianwen-1, probably because the geographic locations and seasons are close to each other, so the excitation sources are comparable. For a detailed comparison of parameters, please refer to Table 1.

The λ_z of the IGW in the southern hemisphere is 6.7 km, and $\omega \approx f$.

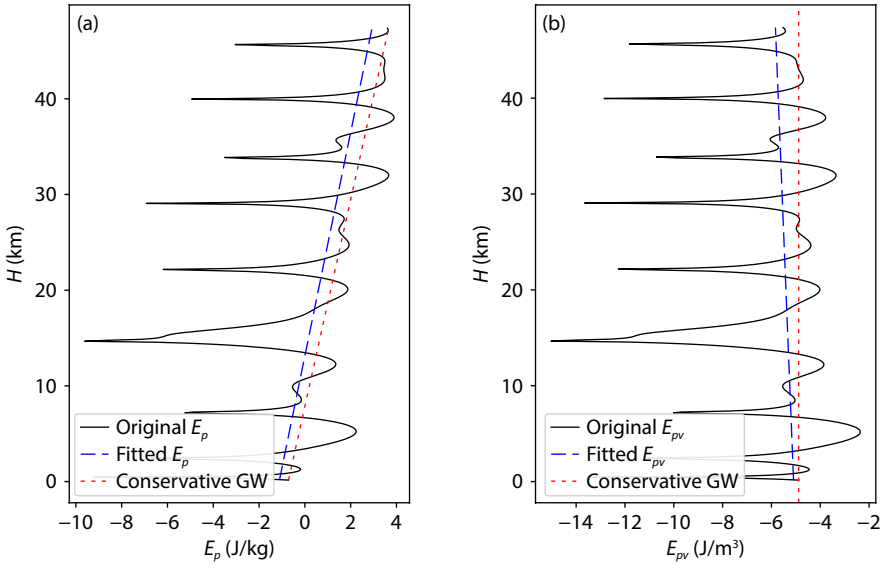

Figure 4. E_p (a) and E_{pv} (b) with altitude for Tianwen-1.

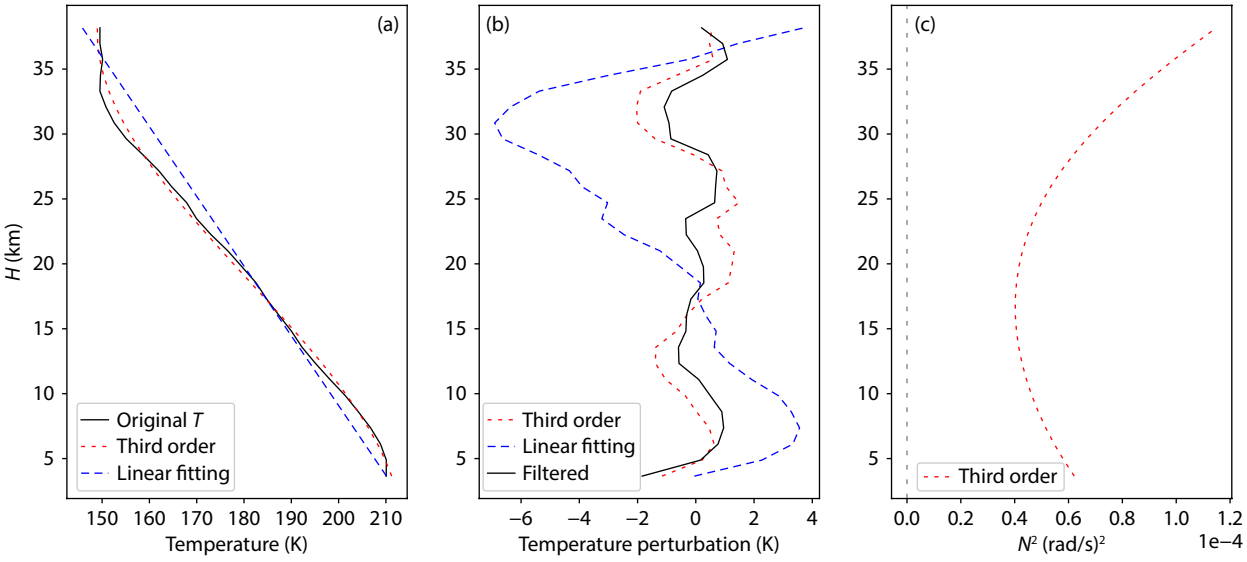

Figure 5. T (a), T' (b), and N^2 (c) with altitude for the MGS in the northern hemisphere (Profile 2).

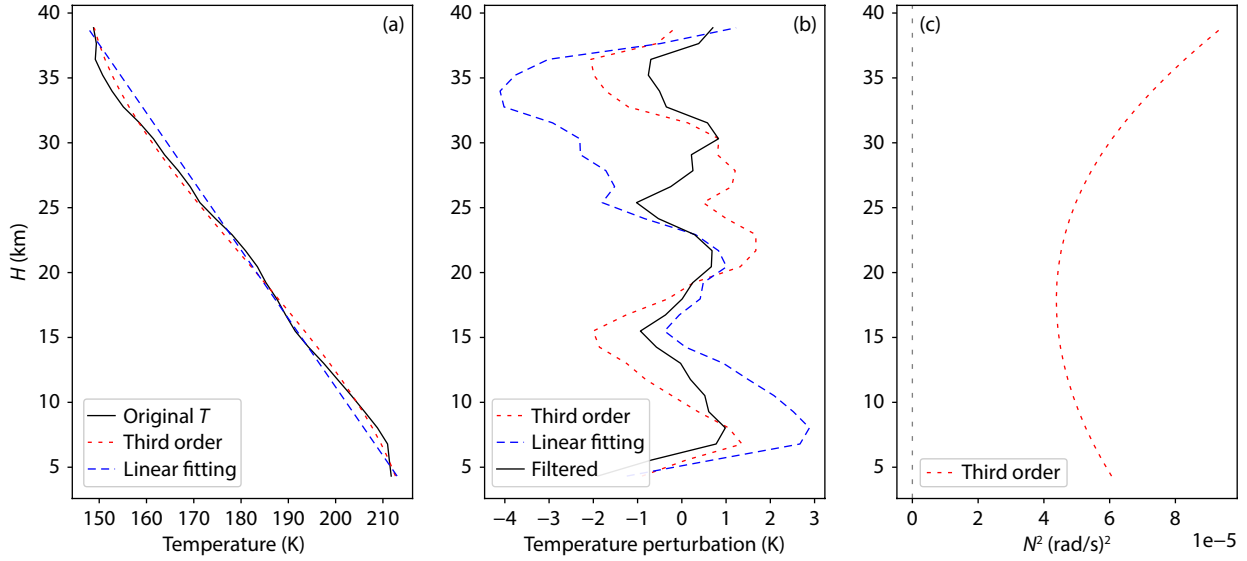

Figure 6. T (a), T' (b), and N^2 (c) with altitude for the MGS in the northern hemisphere (Profile 3).

Compared with the northern hemisphere detected by Tianwen-1 and the MGS, the IGW has a smaller λ_z and a larger N^2, as shown in Figure 7. The T' of the IGW is larger than that in Figures 5b and 6b, which means a larger relative amplitude. The reason could be that the terrain is higher and the temperature is lower in the southern hemisphere. Being a significant excitation source of IGWs, topography, especially in areas with considerable topographic variation, is more likely to trigger the generation of IGWs. These differences naturally lead to differences in the IGW parameters extracted.

The parameters of the IGWs and their associated uncertainties for the selected profiles are presented in Table 1. As shown in the table, the relative uncertainty of λ_z of the MGS is substantially larger than that of Tianwen-1. The $\delta\lambda_z/\lambda_z$ is proportional to the vertical resolution δh of the data. According to Pätzold et al. (2004), the vertical resolution of the X-band RO data is approximately 0.3 km. Both the MGS and Tianwen-1 data utilize X-band RO. However, the MGS has sampling intervals of ~1 km whereas Tianwen-1's sampling intervals are as fine as ~0.1 km. Consequently, the vertical resolution δh of MGS can only achieve approximately 1 km, whereas that of Tianwen-1 can reach up to 0.3 km. Since the term $\delta N^2/N^2$ is the primary contributor to the relative uncertainty in a_e, which significantly influences the uncertainty of other IGW parameters, and given its minimal relationship with δh, the uncertainties of other IGW parameters extracted from the MGS and Tianwen-1 do not differ significantly.

Regarding IGW dissipation, the northern hemisphere of the MGS exhibits greater dissipation compared to Tianwen-1, while the southern hemisphere shows slightly less dissipation. Additionally, the H of the southern hemisphere is much lower than that of both Tianwen-1 and the northern hemisphere of the MGS, which could be attributed to the overall high terrain and low temperature of the southern hemisphere.

In comparison to other studies employing similar parameter

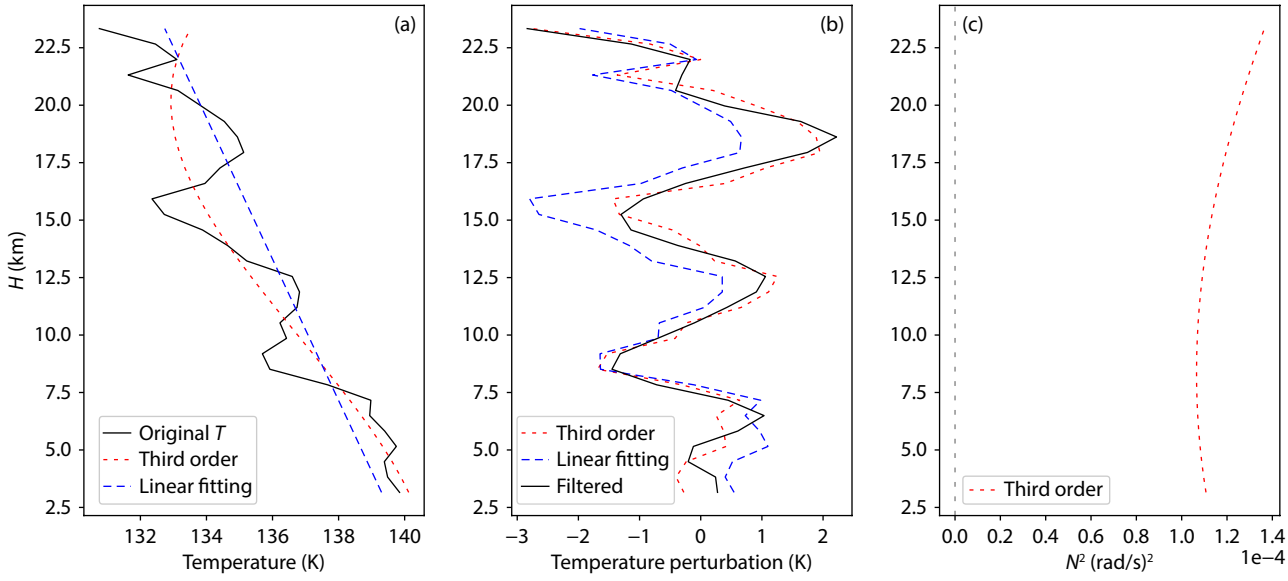

Figure 7. T (a), T' (b), and N^2 (c) with altitude for the MGS in the southern hemisphere.

extraction methods, such as Gubenko et al. (2015), the relative uncertainties of IGWs in this study are smaller. The primary reasons for these smaller uncertainties are as follows: First, regarding the data, this study utilizes a wider altitude range and denser sampling from Tianwen-1. Second, in terms of the spectral analysis method, Gubenko et al. (2015) employed a Fourier transformation, which is suitable only for evenly spaced data, whereas this study utilizes Lomb−Scargle spectral analysis, capable of analyzing nonuniformly sampled data. This approach avoids additional interpolation, thereby eliminating the introduction of artificial errors. Finally, concerning the parameter extraction method, Gubenko et al. (2015) assumed $m \gg 1/2H$ when extracting the horizontal wavelength of IGWs, ignoring the $1/2H$ term, despite the fact that m is not significantly greater than $1/2H$. In this study, we consider the $1/2H$ term and account for the differences in H, resulting in more reliable parameter extraction.

4. Conclusions

Based on the RO data from Tianwen-1 and the MGS, key parameters of IGWs are extracted from the occultation temperature profiles. Results show that the vertical wavelengths λ_z of the Martian IGWs range from 6 to 13 km. The intrinsic frequencies ω of these IGWs are very close to the inertial frequency f, which are typical low-frequency inertial IGWs. The horizontal wavelengths λ_h are longer than their vertical wavelengths λ_z, and their propagation directions are almost vertical. The kinetic energy densities E_k are ~1–2 orders larger than the potential energy densities E_p, and the velocity perturbations caused by IGWs are larger, whereas the temperature perturbations are smaller.

Compared with the IGWs of the MGS in the northern hemisphere, the relative amplitude a_e and potential energy density E_p of the IGWs of Tianwen-1 and the MGS in the southern hemisphere are both larger, indicating stronger IGW activity. In addition, the variable H_{pv} corresponding to Tianwen-1 is larger, indicating that the dissipation of these IGWs is smaller. The H_{pv} in the southern hemisphere of the MGS is also slightly larger than that in the northern hemisphere, and the degree of IGW dissipation is slightly smaller, which may be related to its larger buoyancy frequency N^2. The larger the N^2, the more stable the background atmosphere, and the more conducive it is to the propagation of IGWs. The larger N^2 may be related to the overall higher terrain and lower temperature in the southern hemisphere.

These detailed analyses of IGWs enrich our fundamental understanding of Martian atmospheric dynamics and provide essential data for the parameterization in Martian global circulation models. We anticipate carrying out more occultation experiments for advanced scientific research.

Acknowledgments

This work is funded by the National Natural Science Foundation of China (Grant Nos. 42174192, 12241101, and 91952111). We thank the MGS team for supporting data, which is public and available at https://atmos.nmsu.edu/PDS/data/mors_1101/tps/.

References

Acuña, M. H., Connerney, J. E., Ness, N. F., Lin, R. P., Mitchell, D., Carlson, C. W., McFadden, J., Anderson, K. A., Reme, H., … Cloutier, P. (1999). Global distribution of crustal magnetization discovered by the Mars Global Surveyor MAG/ER experiment. *Science*, *284*(5415), 790–793. https://doi.org/10.1126/science.284.5415.790

Ando, H., Imamura, T., and Tsuda, T. (2012). Vertical wavenumber spectra of gravity waves in the Martian atmosphere obtained from *Mars Global Surveyor* radio occultation data. *J. Atmos. Sci.*, *69*(9), 2906–2912. https://doi.org/10.1175/JAS-D-11-0339.1

Creasey, J. E., Forbes, J. M., and Hinson, D. P. (2006). Global and seasonal distribution of gravity wave activity in Mars' lower atmosphere derived from MGS radio occultation data. *Geophys. Res. Lett.*, *33*(1), L01803. https://doi.org/10.1029/2005gl024037

Creasey, J. E. (2012). Gravity waves and their effects on the mean state and variability of Mars' atmosphere [Ph.D. thesis]. Boulder: University of Colorado.

Fritts, D. C., and Alexander, M. J. (2003). Gravity wave dynamics and effects in the middle atmosphere. *Rev. Geophys.*, *41*(1), 3. https://doi.org/10.1029/2001RG000106

Fritts, D. C., Wang, L., and Tolson, R. H. (2006). Mean and gravity wave structures

and variability in the Mars upper atmosphere inferred from Mars Global Surveyor and Mars Odyssey aerobraking densities. *J. Geophys. Res.: Geophys. Res.*, *111*(A12), 304–317. https://doi.org/10.1029/2006ja011897

Geller, M. A., and Gong, J. (2010). Gravity wave kinetic, potential, and vertical fluctuation energies as indicators of different frequency gravity waves. *J. Geophys. Res.: Atmos.*, *115*(D11), D11111. https://doi.org/10.1029/2009jd012266

Gröller, H., Montmessin, F., Yelle, R. V., Lefèvre, F., Forget, F., Schneider, N. M., Koskinen, T. T., Deighan, J., and Jain, S. K. (2018). MAVEN/IUVS stellar occultation measurements of Mars atmospheric structure and composition. *J. Geophys. Res.: Planets*, *123*(6), 1449–1483. https://doi.org/10.1029/2017JE005466

Gubenko, V. N., Pavelyev, A. G., and Andreev, V. E. (2008). Determination of the intrinsic frequency and other wave parameters from a single vertical temperature or density profile measurement. *J. Geophys. Res.: Atmos.*, *113*(D8), D08109. https://doi.org/10.1029/2007jd008920

Gubenko, V. N., Pavelyev, A. G., Salimzyanov, R. R., and Pavelyev, A. A. (2011). Reconstruction of internal gravity wave parameters from radio occultation retrievals of vertical temperature profiles in the Earth's atmosphere. *Atmos. Meas. Tech. Discuss.*, *4*(2), 1397–1425. https://doi.org/10.5194/amtd-4-1397-2011

Gubenko, V. N., Kirillovich, I. A., and Pavelyev, A. G. (2015). Characteristics of internal waves in the Martian atmosphere obtained on the basis of an analysis of vertical temperature profiles of the *Mars Global Surveyor* mission. *Cosmic Res.*, *53*(2), 133–142. https://doi.org/10.1134/S0010952515020021

He, Y., Zhu, X. Q., Sheng, Z., Zhang, J., Zhou, L. S., and He, M. Y. (2021). Statistical characteristics of inertial gravity waves over a tropical station in the Western Pacific based on high-resolution GPS radiosonde soundings. *J. Geophys. Res.: Atmos.*, *126*(11), e2021JD034719. https://doi.org/10.1029/2021JD034719

Hu, X., Wu, X. C., Song, S. L., Ma, M. L., Zhou, W. L., Xu, Q. C., Li, L., Xiao, C. Y., Li, X., … Li, Z. (2022). First observations of Mars atmosphere and ionosphere with Tianwen-1 radio-occultation technique on 5 August 2021. *Remote Sens.*, *14*(11), 2718. https://doi.org/10.3390/rs14112718

Ji, Q. Q., Zhu, X. Q., Sheng, Z., and Tian, T. (2022). Spectral analysis of gravity waves in the Martian thermosphere during low solar activity based on MAVEN/NGIMS observations. *Astrophys. J.*, *938*(2), 97–109. https://doi.org/10.3847/1538-4357/ac8d07

Le, H. J., Liu, L. B., Chen, Y. D., and Zhang, H. (2022). The north–south asymmetry of Martian ionosphere and thermosphere. *J. Geophys. Res.: Planets*, *127*(6), e2021JE007143. https://doi.org/10.1029/2021JE007143

Lian, Y., and Yelle, V. R. (2019). Damping of gravity waves by kinetic processes in Jupiter's thermosphere. *Icarus*, *329*, 222–245. https://doi.org/10.1016/j.icarus.2019.04.001

Liu, X., Xu, J. Y., and Yue, J. (2020). Global static stability and its relation to gravity waves in the middle atmosphere. *Earth Planet. Phys*, *4*(5), 504–512. https://doi.org/10.26464/epp2020047

Medvedev, A. S., and Yiğit, E. (2019). Gravity waves in planetary atmospheres: Their effects and parameterization in global circulation models. *Atmosphere*, *10*(9), 531–554. https://doi.org/10.3390/atmos10090531

Nappo, C. J. (2013). *An Introduction to Atmospheric Gravity Waves* (2nd ed). Waltham, Massachusetts: Academic Press.

Pätzold, M., Neubauer, F. M., Carone, L., Hagermann, A., Stanzel, C., Häusler, B., Remus, S., Selle, J., Hagl, D., … Dehant, V. (2004). MaRS: Mars express orbiter radio science. In A. Wilson (Ed.), *Mars Express: The Scientific Payload* (pp. 141–163). Noordwijk, Netherlands: ESA Publications Division.

Ratnam, M. V., Babu, A. N., Rao, V. V. M. J., Rao, S. V. B., and Rao, D. N. (2008). MST radar and radiosonde observations of inertia-gravity wave climatology over tropical stations: Source mechanisms. *J. Geophys. Res.: Atmos.*, *113*(D7), D07109. https://doi.org/10.1029/2007jd008986

Saunders, W. R., Person, M. J., and Withers, P. (2021). Observations of gravity waves in the middle atmosphere of Mars. *Astron. J.*, *161*(6), 280–300. https://doi.org/10.3847/1538-3881/abf1ef

Skopovi, I., and Akylas, T. R. (2007). The role of buoyancy–frequency oscillations in the generation of mountain gravity waves. *Theor. Comput. Fluid Dyn.*, *21*(6), 423–433. https://doi.org/10.1007/s00162-007-0061-2

Wang, L., and Geller, A. M. (2003). Morphology of gravity-wave energy as observed from 4 years (1998–2001) of high vertical resolution U. S. radiosonde data. *J. Geophys. Res.: Atmos.*, *108*(D16), 4489. https://doi.org/10.1029/2002JD002786

Wu, Z. P., Li, J., Li, T., Cui, J. (2021). The dust storm and its interaction with atmospheric waves on Mars. *Rev. Geophys. Planet. Phys.* (in Chinese), 52(4): 402–415. https://doi.org/10.19975/j.dqyxx.2021-022

Xiao, C. Y., and Hu, X. (2010). Analysis on the global morphology of stratospheric gravity wave activity deduced from the COSMIC GPS occultation profiles. *GPS Solut.*, *14*(1), 65–74. https://doi.org/10.1007/s10291-009-0146-z

Xiao, L., Xiao, C. Y., Hu, X., Wu, X. C., Wang, Z. W., and Wu, X. Q. (2024). Progress of radio occultation exploration of Mars. *Rev. Geophys. Planet. Phys.* (in Chinese), *55*(2), 164–174. https://doi.org/10.19975/j.dqyxx.2022-083

Zeng, X. Y., and Zhong, G. (2024). Analysis of gravity wave activity during stratospheric sudden warmings in the northern hemisphere. *Earth Planet. Phys*, *8*(2), 415–422. https://doi.org/10.26464/epp2024007

Zhang, J., Ji, Q. Q., Sheng, Z., He, M. Y., He, Y., Zuo, X. J., He, Z. F., Qin, Z. L., and Wu, G. Y. (2023). Observation based climatology Martian atmospheric waves perturbation datasets. *Sci. Data*, *10*(1), 4. https://doi.org/10.1038/s41597-022-01909-y

Zhang, S. J., Ping, J. S., Hong, Z. J., Han, T. T., and Mao, X. F. (2009). Detection of the martian atmosphere and ionosphere using spacecraft-earth radio occultation. *Phys*, *38*(10), 722–728. https://doi.org/10.3321/j.issn:0379-4148.2009.10.005

Zhao, W. B., Hu, X., Yan Z. A., Pan, W. L., Guo, W. J., Yang, J. F., Du, X. Y. (2022). Atmospheric gravity wave potential energy observed by Rayleigh lidar above Jiuquan (40° N, 95° E), China. *Atmosphere*, *13*(7), 1098–1107. https://doi.org/10.3390/atmos13071098